Articles
https://doi.org/10.1038/s41560-017-0048-1
nature energy

Potential-sensing electrochemical atomic force microscopy for in operando analysis of watersplitting catalysts and interfaces

Michael R. Nellist[1], Forrest A. L. Laskowski[1], Jingjing Qiu[1], Hamed Hajibabaei[2], Kevin Sivula[3], Thomas W. Hamann[2] and Shannon W. Boettcher[1]*

Heterogeneous electrochemical phenomena, such as (photo)electrochemical water splitting to generate hydrogen using semiconductors and/or electrocatalysts, are driven by the accumulated charge carriers and thus the interfacial electrochemical potential gradients that promote charge transfer. However, measurements of the "surface" electrochemical potential during operation are not generally possible using conventional electrochemical techniques, which measure/control the potential of a conducting electrode substrate. Here we show that the nanoscale conducting tip of an atomic force microscope cantilever can sense the surface electrochemical potential of electrocatalysts in operando. To demonstrate utility, we measure the potential-dependent and thickness-dependent electronic properties of cobalt (oxy)hydroxide phosphate (CoPi). We then show that CoPi, when deposited on illuminated haematite (α -Fe_2O_3) photoelectrodes, acts as both a hole collector and an oxygen evolution catalyst. We demonstrate the versatility of the technique by comparing surface potentials of CoPi-decorated planar and mesoporous haematite and discuss viability for broader application in the study of electrochemical phenomena.

Photoelectrochemical water-splitting enables the direct conversion and storage of solar energy into energy-dense chemical fuel, H_2[1]. Significant effort has been devoted to develop earth-abundant material systems to drive water splitting, for example water-oxidizing photoanodes made from nanostructured metaloxide light absorbers with catalytic surface layers[2–5]. Understanding the interfacial charge-transfer processes for these systems, specifically the role of the catalyst layer in the enhancement of the oxygen evolution reaction (OER), has been a major challenge[6]. For example, it has been proposed that the catalyst increases band bending in the semiconductor[7,8], improves charge separation in the semiconductor[9] or simply enables more facile OER kinetics[10,11]. Improving the performance of catalyzed photoanodes requires a detailed understanding of the system's fundamental electronic processes. A major roadblock is that the charge state, or surface electrochemical potential, of the catalyst layer cannot easily be measured directly by standard (photo)electrochemical techniques that rely only on an ohmic back contact to the semiconductor.

To directly probe charge-transfer processes in catalyst-coated photoanodes, we previously developed a "dual-working-electrode" (DWE) technique[12,13] where a thin, electrolyte-permeable, Au layer is deposited on the catalyst. The layer is used as a second working electrode to sense or control the voltage and/or current at the catalyst surface. We initially studied model TiO_2 semiconductors coated with Ni(Fe) (oxy)hydroxide catalysts and showed that photogenerated holes accumulate in the catalyst layer, oxidizing it to potentials where catalytic water oxidation occurs. Because the catalyst is permeable to electrolyte, the effective barrier height at the catalyst–semiconductor junction increases as the catalyst is oxidized; we termed this an "adaptive junction"[13–15]. The technique was further applied to photoanodes of Si, a model low-bandgap absorber, which illustrated that the need for a non-porous protection layer, in this case metallic Ni, precluded such adaptive behaviour[16]. Recently, DWE photoelectrochemistry of $Ni_{0.8}Fe_{0.2}O_x$-coated planar α -Fe_2O_3 was enabled by using very smooth spin-coated catalyst layers (< 1 nm root-mean-square roughness)[17].

While a powerful tool to understand charge-transfer processes in planar model systems with uniform catalyst layers, the DWE approach is limited. Application of the second working electrode layer to the top of a catalyst with imperfect or non-uniform coverage results in direct electrical shorting to the underlying semiconductor. This has prevented the study of highly structured semiconductors, patterned catalyst architectures, or photoanodes with (photo)electrodeposited catalyst films that crack when they are removed from the electrolyte and dried. A more versatile and, ideally, spatially resolved potential-sensing technique is needed.

Scanning electrochemical potential microscopy, wherein a piezo actuator and a nanometer potential probe can be used to measure the potential gradient of an electrical double layer as the probe approaches a biased conductive surface[18–21], provides one possible route to measure surface potentials in situ. Scanning electrochemical potential microscopy has been used to map high-resolution images in constant potential mode, an analogue of electrochemical scanning tunneling microscopy which operates in constant current mode[22–24]. Scanning electrochemical potential microscopy imaging, however, conflates topography with

[1] Department of Chemistry and Biochemistry, Materials Science Institute, University of Oregon, Eugene, OR, USA. [2]Department of Chemistry, Michigan State University, East Lansing, MI, USA. [3]Laboratory for Molecular Engineering of Optoelectronic Nanomaterials, École Polytechnique Fédérale de Lausanne (EPFL), Lausanne, Switzerland. *e-mail: swb@uoregon.edu

potential, which makes it difficult to apply to systems where both the surface topography and potential are unknown, such as catalyst-coated photoelectrodes.

Other groups have worked to extend Kelvin-probe force microscopy to liquid environments for nanoscale potential sensing, but these techniques are complicated by mobile ions in solution. This has limited their application to non-polar liquids[25], pure water[26,27] or low-concentration electrolyte (< 10 mM) solutions[28,29]—conditions that are not representative of most practical (photo)electrochemical environments.

Here we demonstrate a contact-based potential-sensing electrochemical atomic force microscopy (PS-EC-AFM) technique to directly measure the surface electrochemical potential in heterogeneous electrochemical systems in operando. We define in operando in the context of semiconductor photoelectrochemistry as where the sample is illuminated, under bias, passing photocurrent and in a practical electrolyte solution. We demonstrate the utility of PS-ECAFM by measuring operating surface potentials in two prototypical (photo)electrochemical systems—cobalt (oxyhydroxide) phosphate (CoPi) electrocatalyst films[30,31] on conducting glass electrodes and CoPi on haematite (α-Fe_2O_3) semiconductor photoelectrodes. We show that CoPi is a good electrical conductor only when oxidized to potentials anodic of the nominally Co^{2+}/Co^{3+} redox wave. When CoPi is deposited on haematite, we show that it collects photogenerated holes from the haematite surface and charges to a potential sufficient to drive water oxidation at the (simultaneously measured) photocurrent density. These measurements directly demonstrate the role of CoPi as both a hole-collecting contact and an electrocatalyst for water oxidation.

Direct measurement of electrocatalyst surface potentials

For potential sensing, we employ a conductive nanotip of an otherwise electrically insulated atomic-force-microscope (AFM) cantilever (Fig. 1a)[32,33]. The tip is placed in direct contact with the sample. As an AFM-based technique, force feedback is used to control tip–substrate interactions through cantilever deflection. This allows a stable electrical connection between the substrate and the AFM nanoelectrode potential-sensing tip, without damaging the catalyst or AFM tip through excessive force. The small area over which the tip interacts with the electrolyte ($\sim 10^{-9}$ cm^2) minimizes capacitive and surface electrochemical processes that may prevent accurate measurement of the catalyst potential. The Fermi level of the catalyst and the tip are assumed to be in equilibrium, enabling the catalyst surface potential to be probed via the tip (Fig. 1b).

To demonstrate the viability of the potential-sensing technique, we first studied CoPi deposited on a conductive ITO substrate. Despite its wide use, little is known about the electrical properties of CoPi. Recent reports have suggested that there are potential losses related to charge transport through the film at sufficiently high current densities[34,35]. Thus, even when controlling the substrate potential through a potentiostat, the electrochemical potential driving oxygen evolution at the catalyst surface remains uncertain.

PS-EC-AFM measurements were made using a custom EC-AFM cell and stage that allowed for bottom illumination with a 405 nm light-emitting diode, an Ag/AgCl reference electrode and a Pt counter-electrode (Supplementary Figure 1). A high-impedance (1 TΩ) sense lead of the potentiostat was used to measure the tip potential, V_{tip} (Supplementary Figure 2) through the conductive AFM probe. The setup was tested by sensing V_{tip} when the tip was in contact with an Au substrate whose potential, V_{sub}, was controlled using the first working electrode of the potentiostat. V_{tip} tracked V_{sub} exactly at a contact force of ~25 nN (Supplementary Figure 3).

CoPi films were deposited on an ITO substrate from a 0.5 mM aqueous $Co(NO_3)_2$ solution at an anodic current density of 50 μA cm^{-2} for 10–30 min. Catalyst loading was monitored by the integration of the Co^{2+}/Co^{3+} reduction wave. The exposed conductive AFM tip was brought into contact with the ITO or catalyst-coated ITO and the surface was imaged using a

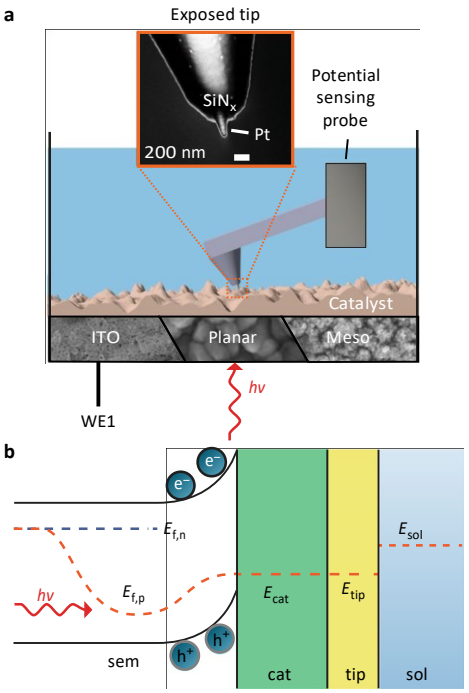

Fig. 1 | AFM method to measure catalyst surface potential during (photo) electrochemical experiments. a, The potential-sensing electrochemical AFM setup with the cantilever, fully electrically insulated except for the exposed nanotip, serving as a potential probe. The inset is an electron micrograph of the AFM tip used. The blue color represents electrolyte. The approach allows for the study of a wide range of (photo)electrochemical structures in operando, including electrodeposited catalysts on conducting indium tin oxide (ITO), planar haematite and nano/mesostructured haematite, connected to the circuit via the working electrode (WE1). **b**, Band diagram for an illuminated semiconductor (sem) electrode (for example, Fe_2O_3) coated with a catalyst (cat) layer (for example, CoPi). $E_{f,n}$ and $E_{f,p}$ are the electron and hole quasi-Fermi levels, respectively. E_{cat} and E_{tip} are the Fermi levels of the catalyst and AFM tip (tip), which are assumed to be in equilibrium. E_{sol} is the redox energy of the electrolyte (sol), here given by the thermodynamic potential for the OER, $\varepsilon_{O\,OH2/\quad\quad-}$, multiplied by the electron charge q. The difference between E_{sol} and E_{cat} (divided by q) is the overpotential driving water oxidation.

force-sensitive tapping mode (Fig. 2a,b). The probe was rested on the catalyst surface with an applied force of about 25 nN, which was sufficiently small to prevent damage to the CoPi films (Supplementary Figure 4), and the potential of the ITO was stepped anodically in 100 mV steps. At V_{sub} <0.2 V versus $\varepsilon_{O\,OH2/-}$

(the OER thermodynamic redox potential), V_{tip} was largely unaffected by changes in V_{sub}. When V_{sub} was 0.27 V or more versus $\varepsilon_{O\ OH2/-}$, V_{tip} began closely tracking V_{sub} (Fig. 2c, Supplementary Figure 3). This observation is consistent with the dramatic increase in electrical conductivity that has been observed when $Co(OH)_2$ species are oxidized to nominally CoOOH, supporting the idea that CoPi is composed of Co (oxy)hydroxide nanosheet fragments that are only electrically conductive when oxidized[36,37]. We observe similar behaviour for a range of catalyst loadings (Supplementary Figure 5), although thicker films require less anodic potentials, as measured by the EC-AFM tip, to achieve any given current density (Fig. 2d). This is expected, as CoPi is a volume-active electrocatalyst (i.e. porous and electrolyte permeable)[38]. For the thickest films employed (~125 nm) we measured $V_{sub} - V_{tip}$ =~20 mV at current densities of ~1 mA cm^{-2} (Supplementary Figure 6)—indicative of electrical resistivity losses for transport through the CoPi layer.

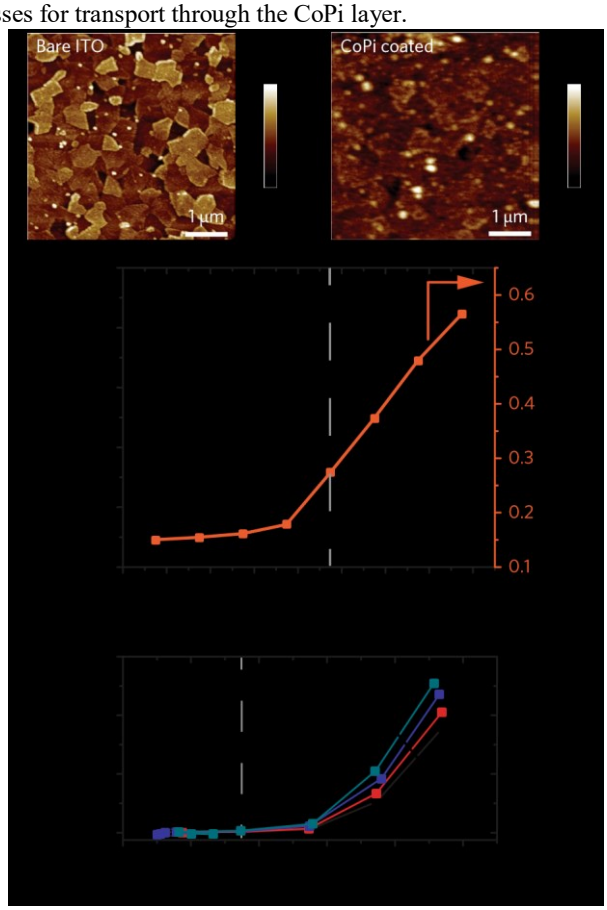

Fig. 2 | Surface potentials of CoPi on an ITO substrate. a, AFM topographic image of bare ITO surface. **b**, AFM topographic image of CoPi-coated ITO surface. **c**, Potential-step experiments performed in 0.1 M aqueous potassium phosphate, buffered to pH 6.9. V_{tip} began tracking V_{sub} at 0.27 V versus $\varepsilon_{O\ OH2/-}$, corresponding to the oxidation of the CoPi. The substrate was held at each potential for up to 1 min, allowing the V_{tip} measurement to stabilize. Voltammetry for the CoPi–ITO is also shown (20 mV s^{-1}). The potential labelled "conductivity switch" is the point where the catalyst is sufficiently oxidized that it becomes electrically conductive and thus its potential can be sensed. **d**, V_{tip} (measured catalyst potential) and the corresponding steady-state currents taken from potential-step experiments as shown in **c**. As the thickness of the catalyst is increased, both the number of catalytically active sites, and the current at a fixed overpotential, increase. Approximate catalyst thicknesses for the black, red, purple and teal lines are 49 nm, 59 nm, 103 nm and 126 nm, respectively.

Some of this potential drop can also be attributed to contact resistance between the catalyst and the probe, which can vary between probes, and with the series resistance through the ITO substrate. We note that at current densities of about 1 mA cm^{-2} or greater oxygen evolving from the sample surface can disrupt the tip, lifting it from the substrate. Because the potential sensing tip is composed of Pt, which is a much worse OER catalyst than CoPi[39], negligible catalytic current flows through the Pt itself, as shown in Supplementary Figure 7.

The measurements on CoPi–ITO demonstrate that PS-ECAFM can accurately measure the applied potential (typically within 25 mV, Supplementary Figure 6) at catalyst surfaces and differentiate between electrically conducting and non-conducting states of the catalyst. The technique further allows for measurement of heterogeneity in electrical properties on the same sample. Supplementary Figure 8 shows that a nanoscale pinhole exposing the Au substrate can be distinguished from electrodeposited Co (oxy)hydroxide catalyst by sensing the surface potential during a cyclic voltammogram. PS-EC-AFM therefore provides direct information about the local electrochemical potential available to drive catalysis. Such information is not readily available by other techniques. Impedance analysis has been used to assess the series resistance of catalytic electrodes, but it is difficult to extract the resistance of the catalyst network for porous catalyst structures where solution permeation through the catalyst promotes mixed ionic–electronic transport[40,41].

Semiconductor–electrocatalyst junction behaviour

The data above demonstrate the prerequisites for applying the measurement to photoelectrodes with porous catalyst overlayers. We use PS-EC-AFM to directly measure the surface potential of CoPi on planar haematite semiconductor photoelectrodes prepared through atomic layer deposition[42]. Following CoPi photoelectrodeposition (50 μ A cm^{-2} under illumination, 6.9 mC cm^{-2} redox-active cobalt, ~100 nm thick), the CoPi–planar haematite was imaged and the conductive nanoelectrode AFM cantilever was rested on the sample surface with an applied force of 25 nN. The substrate potential, V_{sub} (applied to the haematite ohmic back contact, while under illumination), was stepped anodically in 100 mV increments while V_{tip} was measured. From V_{sub} =− 0.8 V to − 0.43 V versus $\varepsilon_{O\ OH2/-}$, V_{tip} did not substantially change, consistent with the catalyst remaining uncharged/reduced (and thus non-conductive) under these conditions. At V_{sub} =− 0.33 V versus $\varepsilon_{O\ OH2/-}$, sufficient photogenerated holes were injected to oxidize the CoPi to the conductive state (Fig. 3a). At this "conductivity-switch" potential, V_{tip} equilibrates to 0.29 V versus $\varepsilon_{O\ OH2/-}$ (the potential of the catalyst). The catalyst potential build-up is driven by the system photovoltage (V_{ph}), which is given by $V_{ph} = V_{tip} - V_{sub}$ =0.62 V. For the catalyst loadings used here, the potential loss through the CoPi film should be small relative to the photovoltage.

The technique was further extended to nanostructured haematite synthesized by atmospheric-pressure chemical vapor deposition[43,44]. These samples are rougher than the atomic-layerdeposited "planar" haematite and contain substantial mesoporosity (Supplementary Figure 9 shows scanning electron

microscopy (SEM) and AFM images). Due to sample roughness, measuring the semiconductor–catalyst junction would be impossible using macroscopic DWE techniques that we have employed previously. CoPi was photoelectrodeposited onto the mesostructured haematite (50 μA cm $^{-2}$, under illumination). Compared with planar haematite, higher catalyst loadings (9.1 mC cm^{-2} of redox-active Co, ~140 nm planar-equivalent thickness) were required due to the larger surface area of the mesostructured sample. When loading/film thickness was too low, the probe did not make sufficient electrical contact with the catalyst and the potential could not be reliably sensed.

As in the case of the planar haematite, the probe was rested on the sample surface (force ~25 nN) and V_{sub} was stepped anodically while the steady-state V_{tip} was measured (typically after 1–2 min per step), under illumination. At V_{sub} = − 0.33 V versus $\varepsilon_{O\ OH2/-}$ the CoPi film was oxidized to the conductive state, driven by the photogenerated holes in the haematite. Based on the measured potential of the CoPi film, V_{ph} is about 0.62–0.65 V. We also quantify the photovoltage by comparing V_{sub} at the conductivity switch for CoPi–ITO and CoPi–α- Fe_2O_3 systems. For both planar and mesostructured haematite, the conductivity switch occurred about 0.6 V cathodic of the CoPi–ITO system, consistent with the approximately 0.6 V photovoltage measured directly between the probe tip and substrate.

The ability to measure the surface potential for a catalyst on a photoelectrode allows us to directly test whether steady-state hole current flows through the CoPi layer or whether the water oxidation happens primarily on the haematite surface. This question is important because several recent studies have suggested that the CoPi acts largely as a spectator, which favorably modulates the interface energetics but does not directly drive the OER[7,45,46]. Using PS-EC-AFM, we compare catalyst potentials necessary to drive a given OER current for CoPi–haematite and CoPi–ITO systems (Fig. 4) with nominally the same catalyst loading (as measured by the integration of the Co redox wave). For the CoPi–haematite (planar) system, the catalyst potentials, for a given photocurrent density, are nearly identical to those measured at the same current density for CoPi–ITO in the dark. This demonstrates that the CoPi is charged by photogenerated holes from haematite until it reaches a potential where the rate of CoPi-mediated water oxidation is equal to the steady-state junction photocurrent.

For the mesostructured system, we also observe that the CoPi is charged to potentials where it drives oxygen evolution. However, for a given measured catalyst potential (V_{tip}), the CoPi on ITO passes a slightly smaller *average* current density than the CoPi on haematite. This difference is probably due to the

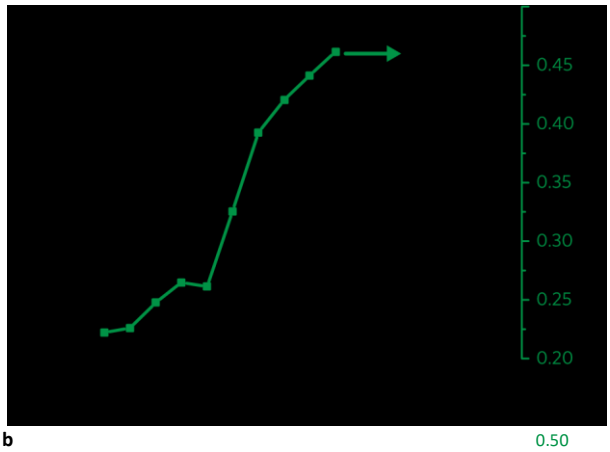

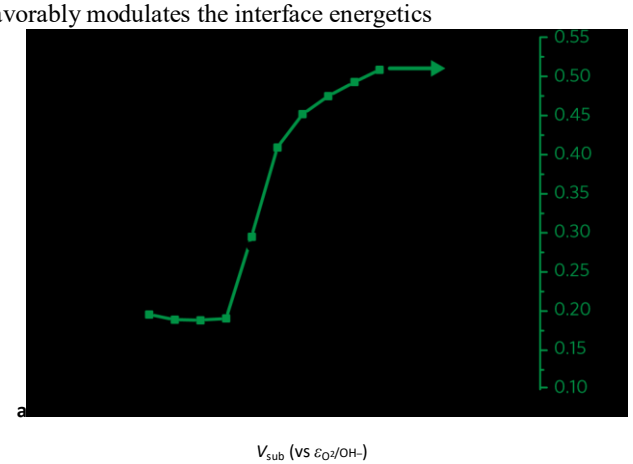

Fig. 3 | In operando PS-eC-AFM potential-step photoelectrochemical experiments. a–b, The measured potential of CoPi on planar haematite (**a**) and the measured potential of CoPi on mesostructured haematite (**b**). The green squares represent the catalyst potential measured by the AFM tip. The simultaneously measured steady-state photocurrent is depicted with black circles. The black lines are voltammograms collected after the potentialstep experiment (20 mV s^{-1}). Both systems were illuminated with 405 nm light calibrated to 27 mW cm^{-2} and collected in 0.1 M potassium phosphate, buffered to pH 6.9. The substrate was held at each potential for up to 2 min, allowing V_{tip} readings and currents to stabilize. In situ AFM images and SEM images of the CoPi-coated haematite, as well as voltammetry of the bare electrodes, are shown in Supplementary Figures 10–12.

morphology differences of the CoPi between the planar ITO and rough haematite. Because light is incident on the backside of the haematite, the less than 10 nm collection length of photogenerated holes

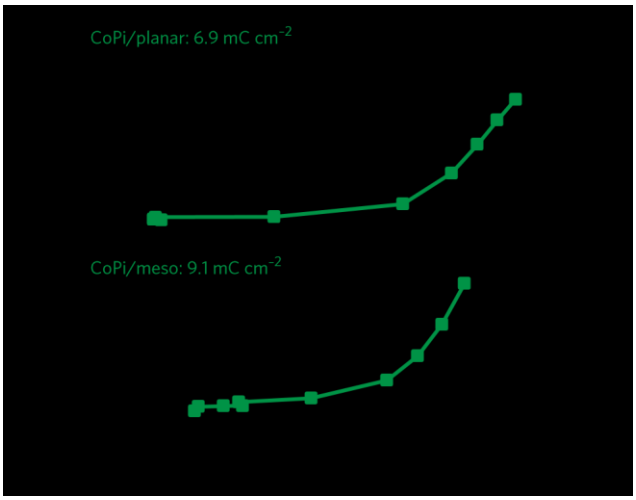

Fig. 4 | CoPi surface potential measurements at given current densities. For illuminated CoPi–planar haematite (top) and illuminated CoPi–mesostructured haematite (bottom), the corresponding dark CoPi–ITO systems shown have nominally the same catalyst loadings. The fact that the curves for the conducting ITO substrates overlay those of the semiconductor photoelectrode substrates indicates that the catalyst is behaving in the same fashion in both cases, independent of whether the holes originate from the ITO or are photogenerated in the haematite. The CoPi acts as a hole-collecting contact and an OER catalyst.

dictates that a large portion of the photocurrent is passed through catalytic particles at the base of the porous haematite film[47,48]. These catalyst particles at the bottom are likely not well electrically integrated with the catalyst film at the top of the porous semiconductor, where AFM sensing occurs. Catalyst regions at the top (which are those sensed by the AFM tip) would therefore sit at less anodic potentials and pass a local current density that is lower than the average measured through the substrate and shown in Fig. 4. Nonetheless, at relevant catalyst potentials of about 0.4–0.45 V versus $\varepsilon_{O\,OH2/-}$ the differences between the average current measured on the CoPi–ITO and CoPi–haematite are only about 5–25% of the photocurrent, again consistent with the hypothesis that photogenerated holes oxidize the CoPi, which then directly drives the OER.

Finally, we note that samples with very high surface roughness may make these measurements more difficult, as the contact area between the tip and surface may change with position. We have, however, reliably measured samples with root-mean-square roughness varying from about 17 to 40 nm (Supplementary Figures 13 and 14). A consistent electrical contact is ensured in these cases by the ability of the AFM to maintain a constant contact force.

Conclusions

We report a PS-EC-AFM technique that enables the probing of the electrical and interfacial properties of heterogeneous electrochemical systems. This allows investigation in operando of electrodeposited catalysts such as CoPi—a material that was not able to be studied by macroscopic potential-sensing techniques previously used. We obtain insight into CoPi electrical conductivity, as well as demonstrating a route to interrogate the role of CoPi on haematite photoanodes. We show that for both planar and mesostructured haematite samples the CoPi is oxidized to a sufficiently high potential to drive water oxidation at a rate commensurate with the junction photocurrent. These data therefore show that CoPi acts as a hole-collecting contact and oxygen evolution catalyst. These results thus add substantially to previous studies, where in some cases CoPi was thought only to improve band bending and/or surface passivation while the OER predominantly occurred on the semiconductor surface. The results here do not rely on modelling, fitting or indirect optical measurements. Since the approach is versatile (and can be applied with any device-fabrication strategy), it may be further used to elucidate the roles of catalyst thickness, morphology and semiconductor structure in semiconductor photoelectrodes.

The PS-EC-AFM technique should be applicable in the study of other electrochemical systems. Because it is based on a scanning-probe platform, the technique is suited for understanding heterogeneity in surface or interface electrochemical response (although not fully exploited in this work, our preliminary results in Supplementary Figures 8 and 15 indicate that this is possible). We have recently hypothesized the presence of a spatially inhomogeneous interface barrier for metallic-Ni-protected Si due to adventitious SiO_2 formation[16]. PS-EC-AFM could provide direct evidence for this hypothesis, which would be difficult to obtain in any other way. The technique could also provide insight into corrosion processes, where there is evidence for nanoscale potential domains[49], as well as new routes to understand the operation of batteries, fuel cells and other electrochemical systems. Measuring and mapping the electrochemical potential in operando could provide insight into such systems' operation and efficiency losses.

Methods

Planar Fe_2O_3. Thin films of Ga_2O_3 and Fe_2O_3 were prepared by atomic layer deposition (Savannah 100, Cambridge Nanotech), using a previously reported procedure[42,48,50,51]. Prior to deposition of Fe_2O_3, an approximately 2-nm-thick Ga_2O_3 underlayer was deposited on F:SnO_2 coated aluminoborosilicate glass substrates (Solaronix, 10 Ω sq^{-1}). The F:SnO_2 substrates were cleaned by sequential sonication in soap, water and isopropyl alcohol for about 15 min followed by drying in a stream of N_2. The Ga_2O_3 was deposited using tris-(dimethylamido)gallium(III) (Strem Chemicals) and H_2O as the Ga precursor and oxidant, respectively, using a modified version of previously reported recipe[52]. Briefly, the Ga precursor was kept at 150 °C and was pulsed for 0.2 s under exposure mode for 8 s, followed by purging for 12 s. Subsequently, H_2O was pulsed for 15 ms with the same exposure–purge times to complete one ALD cycle. A growth rate of about 1.1 Å Ga_2O_3 per cycle was measured by spectroscopic ellipsometry (Horiba Jobin Yvon, Smart-SE) on a Si wafer. The Ga_2O_3-coated F:SnO_2 substrates were then coated with an approximately 30-nm-thick film of Fe_2O_3 by alternating pulses of ferrocene and a combination of water and ozone as the iron precursor and the oxidant, respectively. The ferrocene cylinder was kept at 70 °C and was pulsed for 20 s. Then, an oxidation cycle that included 10 subcycles of H_2O pulsed for 15 ms, followed by a 2 s pulse of ozone, was completed. Each subcycle was separated by purging for a duration of 5 s. After the deposition of Fe_2O_3, films were annealed at 500 °C for 30 min with a ramp rate of 17 °C min^{-1} and allowed to cool to room temperature over 2 h. Subsequently, the films were sintered in a preheated oven at 800 °C for 4 min then quenched to room temperature by removing from the oven.

Mesostructured Fe_2O_3. Films were prepared through atmospheric-pressure chemical vapor deposition, as previously described[43,44]. Briefly, iron pentacarbonyl ($Fe(CO)_5$, Acros 99.5%) and tetraethoxysilane (Aldrich 99.999%, for Si doping) were used as precursors and brought into the gas phase by bubbling argon gas (99.9999%) through each precursor liquid, in separate vials, at different rates: 36 ml min^{-1} for $Fe(CO)_5$ and 30 ml min^{-1} for tetraethoxysilane at 25 °C. A carrier gas stream (dry air, 6 l min^{-1}) was combined with the reactive gas streams and was directed vertically onto a heated substrate (12 mm ×30 mm F:SnO_2 on float glass,

TEC 15 measured to be at 420 °C) through a glass tube of 12 mm inner diameter from a distance of 20 mm. A sheath flux of dry air (total 12 l min^{-1}) was directed around the heater to facilitate the exhaust of the unreacted precursors. The film was deposited over 3 min, giving an approximate film thickness of 500 nm. After cooling, the films were stored in ambient conditions until use. Films were annealed at 350 °C for 10 min prior to electrode preparation to remove any volatile organic compounds on the surface.

Photoelectrochemistry. All experiments were carried out in 0.1 M phosphate buffer adjusted to pH 6.9. Solutions were prepared from 18 MΩ ·cm water. In operando AFM experiments were performed using a custom-modified commercial Bruker EC-AFM cell. The modifications enabled bottom illumination of the haematite as well as the use of a standard Ag/AgCl reference electrode with a saturated KCl filling solution (Pine Research). The potential versus the Ag/AgCl reference electrode was converted to the potential versus the thermodynamic potential for oxygen evolution using the formula V vs $\varepsilon_{O2/OH-} = V$ vs $\varepsilon_{Ag\ AgCl}$ + .0 197 V − .1 23 V +(0 059. V*pH). Substrates were adhered to the homemade Teflon or Kel-F baseplate using double-sided copper tape, electrically connected to a copper wire with silver paint and epoxied to secure the substrate as well as to isolate the conductive components (excluding the substrate) from the electrolyte. A Pt wire lined the inside of the cell and was used for the counter-electrode. The cell was illuminated by a 405 nm light-emitting diode light source (ThorLabs). Light intensities were calibrated using a GaP photodiode to provide the same photocurrent on the GaP as 100 mW cm^{-2} of AM1.5 illumination, that is, about 27 mW cm^{-2} at 405 nm.
The light intensity was verified using a broadband thermopile power meter (Melles Griot). A haematite sample and the Teflon baseplate, as well as the custom-built AFM stage used for photoelectrochemical experiments, are shown in Supplementary Figure 1.

CoPi deposition. Cobalt oxyhydroxide phosphate OER catalysts were deposited from a 0.1 M phosphate buffer at pH 6.9 with 0.5 mM $Co(NO_3)_2$, at a current density of ~50 μ A cm^{-2}. Deposition times were varied, or additional depositions were carried out, to control CoPi loading. Haematite samples were illuminated using a 405 nm light-emitting diode at 27 mW cm^{-2}, as described above. Catalyst loading was monitored by integration of the reduction wave for CoPi on ITO and haematite substrates. AFM and SEM images of CoPi-coated haematite electrodes are shown in Supplementary Figure 11. SEM cross-sections of CoPi-coated mesostructured haematite and ITO are shown in Supplementary Figure 12.
Estimation of CoPi thickness. To estimate the CoPi thickness we started with the relationship defined in ref. [53] based on previous work[54,55],

$$\text{thickness(nm)} = .1\ 5\text{????nmmC}\underline{\text{c}}\text{m}_2\ \text{??????}\ Q_{dep}\text{?????cmmC}_2\ \text{?????}.$$

Q_{dep} is the charge per cm^2 passed during the deposition, with the assumption that all charge passed is used to oxidize Co^{2+}. This assumption holds for slow deposition rates, while faster depositions may have some percentage of charge used to oxidize water[30,56]. We chose to deposit at a constant current density of 50 μ A cm^{-2} because of the speed of catalyst deposition, as well as the ability to maintain similar deposition parameters for a variety of substrates (ITO, planar and mesostructured haematite). Therefore, we used the integration of the reduction wave to directly compare loadings. Since it has been suggested that only 10% of the CoPi film is redox active[34], we replaced Q_{dep} with 10 Q_{red}, as shown below, where Q_{red} is the integrated charge in the CoPi reduction wave:

$$\text{thickness(nm)} = .1\ 5\text{????nmmC}\underline{\text{c}}\text{m}_2\ \text{??????}\ 10Q_{red}\text{?????cmmC}_2\ \text{?????}.$$

Measurements. A Dimension ICON atomic force microscope (Bruker) was used both for topographical imaging of bare substrates in air (tapping mode, TESPA V2 probes) and for in operando electrochemical work (PeakForce tapping mode, scanning electrochemical microscope module, scanning electrochemical microscope probes). A Bio-Logic SP300 potentiostat fitted with an ultralowcurrent option was used for (photo)electrochemical measurement. For potentialsensing DWE measurements, the counter-electrode potential-sense probe was separated from the counter-electrode and attached to the AFM tip (through the strain release module). The scanning electrochemical microscope probe was held on the sample surface using the point-and-shoot function in the Bruker software. All the results reported were reproducible and representative of the typical behaviour observed for each system (Supplementary Figure 14). SEM images were collected using a Zeiss Ultra 55 SEM at 5 keV beam energy and with a 30 μ m aperture.

Data availability. The data that support the plots within this paper and other findings of this study are available from the corresponding author upon reasonable request.

Received: 14 June 2017; Accepted: 25 October 2017;
Published online: 11 December 2017

References

1. Walter, M. G. et al. Solar water splitting cells. *Chem. Rev.* **110**, 6446–6473 (2010).
2. Sivula, K. & Van de Krol, R. Semiconducting materials for photoelectrochemical energy conversion. *Nat. Rev. Mater.* **1**, 15015 (2016).
3. Zandi, O. & Hamann, T. W. The potential versus current state of water splitting with hematite. *Phys. Chem. Chem. Phys.* **17**, 22485–22503 (2015).
4. Sivula, K. Metal oxide photoelectrodes for solar fuel production, surface traps, and catalysis. *J. Phys. Chem. Lett.* **4**, 1624–1633 (2013).
5. Cowan, A. J. & Durrant, J. R. Long-lived charge separated states in nanostructured semiconductor photoelectrodes for the production of solar fuels. *Chem. Soc. Rev.* **42**, 2281–2293 (2013).
6. Montoya, J. H. et al. Materials for solar fuels and chemicals. *Nat. Mater.* **16**, 70–81 (2017).
7. Barroso, M. et al. Dynamics of photogenerated holes in surface modified α -Fe_2O_3 photoanodes for solar water splitting. *Proc. Natl Acad. Sci. USA* **109**, 15640–15645 (2012).
8. Barroso, M. et al. The role of cobalt phosphate in enhancing the photocatalytic activity of α -Fe_2O_3 toward water oxidation. *J. Am. Chem. Soc.* **133**, 14868–14871 (2011).
9. Klahr, B. M., Gimenez, S., Fabregat-Santiago, F., Bisquert, J. & Hamann, T. W. Photoelectrochemical and impedance spectroscopic investigation of water oxidation with 'Co–Pi'-coated hematite electrodes. *J. Am. Chem. Soc.* **134**, 16693–16700 (2012).
10. Carroll, G. M., Zhong, D. K. & Gamelin, D. R. Mechanistic insights into solar water oxidation by cobalt-phosphate-modified α -Fe_2O_3 photoanodes. *Energy Environ. Sci.* **8**, 577–584 (2015).
11. Carroll, G. M. & Gamelin, D. R. Kinetic analysis of photoelectrochemical water oxidation by mesostructured Co-Pi/α -Fe_2O_3 photoanodes. *J. Mater. Chem. A* **4**, 2986–2994 (2016).
12. Lin, F. & Boettcher, S. W. Adaptive semiconductor/electrocatalyst junctions in water-splitting photoanodes. *Nat. Mater.* **13**, 81–86 (2014).
13. Nellist, M. R., Laskowski, F. A. L., Lin, F., Mills, T. J. & Boettcher, S. W. Semiconductor–electrocatalyst interfaces: theory, experiment, and applications in photoelectrochemical water splitting. *Acc. Chem. Res.* **49**, 733–740 (2016).
14. Lin, F., Bachman, B. F. & Boettcher, S. W. Impact of electrocatalyst activity and ion permeability on water-splitting photoanodes. *J. Phys. Chem. Lett.* **6**, 2427–2433 (2015).
15. Mills, T. J., Lin, F. & Boettcher, S. W. Theory and simulations of electrocatalyst-coated semiconductor electrodes for solar water splitting. *Phys. Rev. Lett.* **112**, 148304 (2014).
16. Laskowski, F. A. L., Nellist, M. R., Venkatkarthick, R. & Boettcher, S. W. Junction behavior of n-Si photoanodes protected by thin Ni elucidated from dual working electrode photoelectrochemistry. *Energy Environ. Sci.* **10**, 570–579 (2017).
17. Qiu, J. et al. Direct in situ measurement of charge transfer processes during photoelectrochemical water oxidation on catalyzed hematite. *ACS Cent. Sci.* **3**, 1015–1025 (2017).
18. Hurth, C., Li, C. & Bard, A. J. Direct probing of electrical double layers by scanning electrochemical potential microscopy. *J. Phys. Chem. C* **111**, 4620–4627 (2007).
19. Yoon, Y. et al. A nanometer potential probe for the measurement of electrochemical potential of solution. *Electrochim. Acta* **52**, 4614–4621 (2007).
20. Yoon, Y., Woo, D., Shin, T., Chung, T. D. & Kang, H. Real-space investigation of electrical double layers. Potential gradient measurement with a nanometer potential probe. *J. Phys. Chem. C* **115**, 17384–17391 (2011).
21. Woo, D., Yoo, J., Park, S., Jeon, I. C. & Kang, H. Direct probing into the electrochemical interface using a novel potential probe: Au(111) electrode/$NaBF_4$ solution interface. *Bull. Korean Chem. Soc.* **25**, 577–580 (2004).
22. Baier, C. & Stimming, U. Imaging single enzyme molecules under in situ conditions. *Angew. Chemie Int. Ed.* **48**, 5542–5544 (2009).

23. Hamou, R. F., Biedermann, P. U., Erbe, A. & Rohwerder, M. Numerical analysis of Debye screening effect in electrode surface potential mapping by scanning electrochemical potential microscopy. *Electrochem. Commun.* **12**, 1391–1394 (2010).
24. Traunsteiner, C., Tu, K. & Kunze-Liebhauser, J. High-resolution imaging of the initial stages of oxidation of Cu(111) with scanning electrochemical potential microscopy. *ChemElectroChem* **2**, 77–84 (2015).
25. Domanski, A. L. et al. Kelvin probe force microscopy in nonpolar liquids. *Langmuir* **28**, 13892–13899 (2012).
26. Collins, L. et al. Probing charge screening dynamics and electrochemical processes at the solid–liquid interface with electrochemical force microscopy. *Nat. Commun.* **5**, 3871 (2014).
27. Collins, L. et al. Kelvin probe force microscopy in liquid using electrochemical force microscopy. *Beilstein J. Nanotechnol.* **6**, 201–214 (2015).
28. Kobayashi, N., Asakawa, H. & Fukuma, T. Nanoscale potential measurements in liquid by frequency modulation atomic force microscopy. *Rev. Sci. Instrum.* **81**, 123705 (2010).
29. Kobayashi, N., Asakawa, H. & Fukuma, T. Dual frequency open-loop electric potential microscopy for local potential measurements in electrolyte solution with high ionic strength. *Rev. Sci. Instrum.* **83**, 33709 (2012).
30. Kanan, M. W. & Nocera, D. G. In situ formation of an oxygen-evolving catalyst in neutral water containing phosphate and Co^{2+}. *Science* **321**, 1072–1075 (2008).
31. Lutterman, D. A., Surendranath, Y. & Nocera, D. G. A self-healing oxygen-evolving catalyst. *J. Am. Chem. Soc.* **131**, 3838–3839 (2009).
32. Huang, Z. et al. PeakForce scanning electrochemical microscopy with nanoelectrode probes. *Microsc. Today* **24**, 18–25 (2016).
33. Nellist, M. R. et al. Atomic force microscopy with nanoelectrode tips for high resolution electrochemical, nanoadhesion and nanoelectrical imaging. *Nanotechnology* **28**, 95711 (2017).
34. Costentin, C., Porter, T. R. & Saveant, J.-M. Conduction and reactivity´ in heterogeneous-molecular catalysis: new insights in water oxidation catalysis by phosphate cobalt oxide films. *J. Am. Chem. Soc.* **138**, 5615–5622 (2016).
35. Andrieux, C. P., Costentin, C., Di Giovanni, C., Saveant, J.-M. & Tard, C.´ Conductive mesoporous catalytic films. Current distortion and performance degradation by dual-phase ohmic drop effects. Analysis and remedies. *J. Phys. Chem. C* **120**, 21263–21271 (2016).
36. Burke, M. S., Kast, M. G., Trotochaud, L., Smith, A. M. & Boettcher, S. W. Cobalt–iron (oxy)hydroxide oxygen evolution electrocatalysts: the role of structure and composition on activity, stability, and mechanism. *J. Am. Chem. Soc.* **137**, 3638–3648 (2015).
37. Burke, M. S. et al. Revised oxygen evolution reaction activity trends for first-row transition-metal (oxy)hydroxides in alkaline media. *J. Phys. Chem. Lett.* **6**, 3737–3742 (2015).
38. Klingan, K. et al. Water oxidation by amorphous cobalt-based oxides: volume activity and proton transfer to electrolyte bases. *ChemSusChem* **7**, 1301–1310 (2014).
39. Jörissen, L. Bifunctional oxygen/air electrodes. *J. Power Sources* **155**, 23–32 (2006).
40. Doyle, R. L. & Lyons, M. E. G. An electrochemical impedance study of the oxygen evolution reaction at hydrous iron oxide in base. *Phys. Chem. Chem. Phys.* **15**, 5224–5237 (2013).
41. Batchellor, A. S. & Boettcher, S. W. Pulse-electrodeposited Ni–Fe (oxy)hydroxide oxygen evolution electrocatalysts with high geometric and intrinsic activities at large mass loadings. *ACS Catal.* **5**, 6680–6689 (2015).
42. Klahr, B. M., Martinson, A. B. F. & Hamann, T. W. Photoelectrochemical investigation of ultrathin film iron oxide solar cells prepared by atomic layer deposition. *Langmuir* **27**, 461–468 (2011).
43. Tilley, S. D., Cornuz, M., Sivula, K. & Grätzel, M. Light-induced water splitting with hematite: improved nanostructure and iridium oxide catalysis. *Angew. Chemie Int. Ed.* **49**, 6405–6408 (2010).
44. Kay, A., Cesar, I. & Grätzel, M. New benchmark for water photooxidation by nanostructured α -Fe_2O_3 films. *J. Am. Chem. Soc.* **128**, 15714–15721 (2006).
45. Ma, Y., Kafizas, A., Pendlebury, S. R., Le Formal, F. & Durrant, J. R. Photoinduced absorption spectroscopy of CoPi on $BiVO_4$: the function of CoPi during water oxidation. *Adv. Funct. Mater.* **26**, 4951–4960 (2016).
46. Ma, Y., Le Formal, F., Kafizas, A., Pendlebury, S. R. & Durrant, J. R. Efficient suppression of back electron/hole recombination in cobalt phosphate surface-modified undoped bismuth vanadate photoanodes. *J. Mater. Chem. A* **3**, 20649–20657 (2015).
47. Kennedy, J. H. & Frese, K. W. Photooxidation of water at α -Fe_2O_3 electrodes. *J. Electrochem. Soc.* **125**, 709–714 (1978).
48. Zandi, O., Schon, A. R., Hajibabaei, H. & Hamann, T. W. Enhanced charge separation and collection in high-performance electrodeposited hematite films. *Chem. Mater.* **28**, 765–771 (2016).
49. Honbo, K. et al. Visualizing nanoscale distribution of corrosion cells by open-loop electric potential microscopy. *ACS Nano* **10**, 2575–2583 (2016).
50. Klahr, B. M., Gimenez, S., Fabregat-Santiago, F., Hamann, T. W. & Bisquert, J.
Water oxidation at hematite photoelectrodes: the role of surface states. *J. Am. Chem. Soc.* **134**, 4294–4302 (2012).
51. Zandi, O. & Hamann, T. W. Enhanced water splitting efficiency through selective surface state removal. *J. Phys. Chem. Lett.* **5**, 1522–1526 (2014).
52. Dezelah, C. L., Niinistö, J., Arstila, K., Niinistö, L. & Winter, C. H. Atomic layer deposition of Ga_2O_3 films from a dialkylamido-based precursor. *Chem. Mater.* **18**, 471–475 (2006).
53. Surendranath, Y., Kanan, M. W. & Nocera, D. G. Mechanistic studies of the oxygen evolution reaction by a cobalt-phosphate catalyst at neutral pH. *J. Am. Chem. Soc.* **132**, 16501–16509 (2010).
54. Risch, M. et al. Cobalt–oxo core of a water-oxidizing catalyst film. *J. Am. Chem. Soc.* **131**, 6936–6937 (2009).
55. Kanan, M. W. et al. Structure and valency of a cobalt-phosphate water oxidation catalyst determined by in situ X-ray spectroscopy. *J. Am. Chem. Soc.* **132**, 13692–13701 (2010).
56. Surendranath, Y., Dinca, M. & Nocera, D. G. Electrolyte-dependent electrosynthesis and activity of cobalt-based water oxidation catalysts. *J. Am. Chem. Soc.* **131**, 2615–2620 (2009).

Acknowledgements

This work was supported by the Department of Energy, Basic Energy Sciences, Award DE-SC0014279. S.W.B also thanks the Sloan and Dreyfus Foundations for additional support. The atomic force microscope was purchased using funds provided by the NSF Major Research Instrumentation Program, Grant DMR-1532225. The growth of the planar haematite electrodes was supported by NSF Award CHE-1664823. F.A.L.L. acknowledges funding from the NSF GRFP, Grant 1309047. We thank Dr Fuding Lin, Dr Michaela B. Stevens, Dr Matthew G. Kast, Dr Sebastian Oener and Lisa J. Enman for helpful conversations, Dr Christian Dette for assistance in preparing figures, Dr Zhuangqun Huang for technical assistance with the AFM and John Boosinger for help designing the electrochemistry cell.

Author contributions

M.R.N. and S.W.B. conceived the experiments and led the project. M.R.N. conducted the in operando studies; M.R.N. and F.A.L.L. prepared (photo)electrodes. H.H. and T.W.H. supplied planar haematite samples and K.S. provided mesostructured haematite samples. M.R.N., J.Q. and S.W.B. wrote the manuscript with input from all authors.

Competing interests

The authors declare no competing financial interests.

Additional information

Supplementary information is available for this paper at https://doi.org/10.1038/s41560-017-0048-1.

Reprints and permissions information is available at www.nature.com/reprints.

Correspondence and requests for materials should be addressed to S.W.B.

Publisher's note: Springer Nature remains neutral with regard to jurisdictional claims in published maps and institutional affiliations.